

MIT Open Access Articles

*Dynamics of convective dissolution from
a migrating current of carbon dioxide*

The MIT Faculty has made this article openly available. **Please share**
how this access benefits you. Your story matters.

Citation: Hidalgo, Juan J., Christopher W. MacMinn, and Ruben Juanes. "Dynamics of Convective Dissolution from a Migrating Current of Carbon Dioxide." *Advances in Water Resources* 62 (December 2013): 511–519. © 2013 Elsevier Ltd.

As Published: <http://dx.doi.org/10.1016/j.adwatres.2013.06.013>

Publisher: Elsevier

Persistent URL: <http://hdl.handle.net/1721.1/101652>

Version: Author's final manuscript: final author's manuscript post peer review, without publisher's formatting or copy editing

Terms of use: Creative Commons Attribution-NonCommercial-NoDerivs License



Dynamics of Convective Dissolution from a Migrating Current of Carbon Dioxide

Juan J. Hidalgo^{a,b}, Christopher W. MacMinn^c, Ruben Juanes^{a,*}

^a*Massachusetts Institute of Technology, Cambridge, Massachusetts, USA*

^b*Institute for Environmental Assessment and Water Research, Spanish National Research Council, Barcelona, Spain*

^c*Yale University, New Haven, Connecticut, USA*

Abstract

During geologic storage of carbon dioxide (CO₂), trapping of the buoyant CO₂ after injection is essential in order to minimize the risk of leakage into shallower formations through a fracture or abandoned well. Models for the subsurface behavior of the CO₂ are useful for the design, implementation, and long-term monitoring of injection sites, but traditional reservoir-simulation tools are currently unable to resolve the impact of small-scale trapping processes on fluid flow at the scale of a geologic basin. Here, we study the impact of solubility trapping from convective dissolution on the up-dip migration of a buoyant gravity current in a sloping aquifer. To do so, we conduct high-resolution numerical simulations of the gravity current that forms from a pair of miscible analogue fluids. Our simulations fully resolve the dense, sinking fingers that drive the convective dissolution process. We analyze the dynamics of the dissolution flux along the moving CO₂-brine interface, in-

*Corresponding author

Email addresses: `jhidalgo@mit.edu` (Juan J. Hidalgo),
`christopher.macminn@yale.edu` (Christopher W. MacMinn), `juan@mit.edu` (Ruben Juanes)

cluding its decay as dissolved buoyant fluid accumulates beneath the buoyant current. We show that the dynamics of the dissolution flux and the macroscopic features of the migrating current can be captured with an upscaled sharp-interface model.

Keywords: CO₂ sequestration, gravity current, convective dissolution, sharp interface model, upscaling

1. Introduction

2 The injection of carbon dioxide (CO₂) into deep saline aquifers is a
3 promising tool for reducing anthropogenic CO₂ emissions [1, 2, 3, 4]. Af-
4 ter injection, the buoyant CO₂ will spread and migrate laterally as a gravity
5 current relative to the denser ambient brine, increasing the risk of leakage
6 into shallower formations through fractures, outcrops, or abandoned wells.

7 One mechanism that acts to arrest and securely trap the migrating CO₂
8 is dissolution of CO₂ into the brine [5]. Dissolved CO₂ is considered trapped
9 because brine with dissolved CO₂ is denser than the ambient brine, and sinks
10 to the bottom of the aquifer. In addition to providing storage security by
11 hindering the return of the CO₂ to the atmosphere, this sinking fluid triggers
12 a hydrodynamic fingering instability that drives convection in the brine and
13 greatly enhances the rate of CO₂ dissolution [6, 7, 8, 9].

14 Although this process of convective dissolution is expected to play a major
15 role in limiting CO₂ migration and accelerating CO₂ trapping [4], the inter-
16 action of convective dissolution with a migrating gravity current remains
17 poorly understood. This is due primarily to the disparity in scales between
18 the long, thin gravity current and the details of the fingering instability. Re-

19 solving these simultaneously has proven challenging for traditional reservoir
20 simulation tools [10]. Upscaled theoretical models [11, 12] and laboratory ex-
21 periments [13, 14] have recently provided some macroscopic insights, but by
22 design these capture only the averaged dynamics of the dissolution process.

23 Here, we study the impact of convective dissolution on the migration of
24 a buoyant gravity current in a sloping aquifer by conducting high-resolution
25 numerical simulations of a pair of miscible analogue fluids. Our simulations
26 fully resolve the small-scale features of the convective dissolution process.
27 We define an average dissolution flux and use it to study the dynamic in-
28 teractions of the fingering instability with the migrating current. We then
29 compare these results with the predictions of an upscaled theoretical model
30 to investigate the degree to which this simple model can capture the macro-
31 scopic features of the migrating current.

32 **2. Analogue fluids**

33 For simplicity, and to focus on the role of convective dissolution, we ne-
34 glect capillarity and assume that the two fluids are perfectly miscible. We
35 adopt constitutive laws for density and viscosity that are inspired by a pair
36 of miscible analogue fluids that have been used to study this problem ex-
37 perimentally [15, 16, 13, 14]. This system captures three key features of the
38 CO₂-brine system: (1) a density contrast that stratifies the pure fluids and
39 drives the migration of the gravity current, (2) an intermediate density max-
40 imum that triggers and drives convective dissolution (discussed below), and
41 (3) a viscosity contrast between the pure fluids that influences the shape and
42 propagation speed of the gravity current.

43 We write the dimensionless density ρ and viscosity μ as functions of the
 44 local concentration c of the buoyant fluid. We scale the concentration c by the
 45 solubility so that $c \in [0, 1]$. Since the analogue fluids have different densities
 46 ($\rho(c = 1) < \rho(c = 0)$), the buoyant one will “float” and migrate above the
 47 denser one. Since they are perfectly miscible, they will be separated by a
 48 transition zone that forms and grows through diffusion, and within which
 49 the local concentration transitions from $c = 0$ to $c = 1$ and the local density
 50 and viscosity vary accordingly.

51 To trigger convective dissolution, the essential feature of the density law
 52 is that it must be a non-monotonic function of concentration with an inter-
 mediate maximum (Fig. 1). This shape introduces a neutral concentration

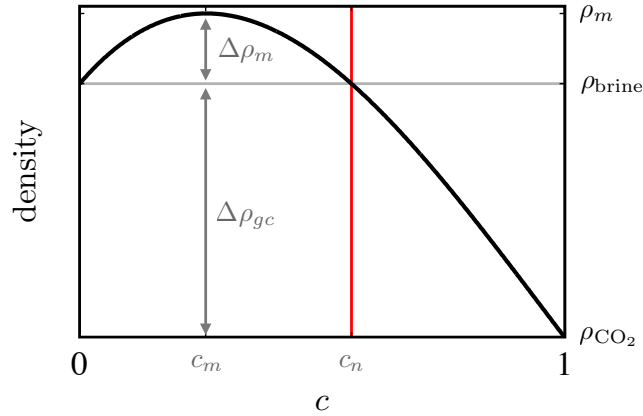


Figure 1: Non-monotonic density law (dimensional) inspired by miscible analogue fluids [15, 16]. The density has a maximum at $c = c_m$. The contour of neutral concentration $c = c_n$ (red line) acts as an interface: mixtures with $c < c_n$ (left of the red line) are denser than the ambient brine and will sink, whereas those with $c > c_n$ (right of the red line) are buoyant relative to the ambient brine and will rise. $\Delta\rho_m$ is the characteristic density difference that drives convective dissolution and $\Delta\rho_{gc}$ is the one that drives the migration of the buoyant gravity current.

53 $c = c_n$ for which the density of the mixture is equal to the density of the
 54 ambient fluid. Fluid with concentration $c > c_n$ (*i.e.*, to the right of c_n)
 55 is less dense than the ambient and tends to float, whereas fluid with con-
 56 centration $c < c_n$ (*i.e.*, to the left of c_n) is *denser* than the ambient and
 57 tends to sink. The contour of neutral concentration within the transition
 58 zone therefore emerges as a natural “interface” between buoyant and sinking
 59 fluids: the fluid above is buoyant and stably stratified (density decreasing
 60 as concentration increases from $c = c_n$ to $c = 1$), the fluid below is dense
 61 and unstably stratified (density decreasing as concentration decreases from
 62 $c = c_n$ to $c = 0$), and diffusion continuously transfers fluid from the stable
 63 region to the unstable region.

64 The concentration $c = c_m$ at which the density maximum occurs plays
 65 the role of a solubility in this system since the density of the underlying fluid
 66 increases toward this value as dissolved buoyant fluid accumulates. Convec-
 67 tive dissolution stops entirely when diffusion at the interface is no longer able
 68 to generate a mixture that is denser than the fluid below it.

69 To make the density law dimensionless, we shift it by the brine density
 70 and scale it by the height of the density maximum so that the dimensionless
 71 brine density is always $\rho(c = 0) = 0$ and the dimensionless density maximum
 72 is always $\rho(c = c_m) = 1$. We represent the density law with a polynomial of
 73 degree three, $\rho(c) = 6.19c^3 - 17.86c^2 + 8.07c$, which has neutral concentration
 74 $c_n = 0.56$, a density maximum at $c_m = 0.26$, and a dimensionless CO₂ density
 75 of $\rho(c = 1) = -3.6$. This density law is qualitatively and quantitatively
 76 similar to the true density law for mixtures of propylene glycol ($c = 0$, brine
 77 analogue) and water ($c = 1$, CO₂ analogue) [16].

78 We choose an exponential constitutive law for the dimensionless viscosity,
79 $\mu(c) = \exp[R(c_m - c)]$, where we have scaled $\mu(c)$ by characteristic viscosity
80 μ_m so that $\mu(c = c_m = 0.26) = 1$. The parameter $R = \ln \mathcal{M}$, where $\mathcal{M} =$
81 $\mu_{\text{brine}}/\mu_{\text{CO}_2} = \mu(c = 0)/\mu(c = 1)$ is the mobility ratio. This viscosity law is
82 qualitatively and quantitatively similar to the true viscosity law for mixtures
83 of propylene glycol and water for $R \approx 3.7$ [16].

84 Since these analogue fluids are perfectly miscible, our results do not in-
85 corporate the various impacts of capillarity, including residual trapping, the
86 development of a capillary fringe, and capillary pressure hysteresis. The
87 absence of capillarity is a limitation in the sense that these analogue fluids
88 cannot capture every aspect of the CO₂-brine system, but it is also an advan-
89 tage in the sense that it allows us to isolate and study convective dissolution
90 as a transport process without these additional complications [15, 16, 13, 14].

91 Capillarity may impact the dynamics of the gravity current. For exam-
92 ple, the gravity current will shrink due to residual trapping along its trailing
93 edge [17, 18, 19]. The formation of a capillary fringe between the CO₂ and the
94 brine may change the shape and reduce the propagation speed of the gravity
95 current [20, 21, 22]. Capillary pressure hysteresis may also reduce the prop-
96 agation speed of the gravity current and even arrest its migration [23, 24].
97 All of these effects can be incorporated into upscaled models for CO₂ migra-
98 tion, but incorporating them into our 2D simulations is less straightforward.
99 These effects would impact the total dissolution rate by changing the length
100 of the “interface” between the two fluids, and by reducing the amount of
101 ambient fluid available for “storing” dissolved CO₂. However, we would not
102 expect them to change the dynamic interactions of migration and dissolution

103 as described here.

104 Capillarity may also have a quantitative impact on the onset and sub-
105 sequent rate of convective dissolution [25, 26, 27]. These effects have never
106 been studied experimentally and are not well understood, but we expect the
107 same qualitative behavior of the dissolution flux (diffusion, onset, convec-
108 tion). Although miscible analogue fluid systems may feature quantitatively
109 different fluxes, they are useful for studying the dynamics of the dissolution
110 flux and its impact on migration.

111 3. Mathematical model

112 We consider a two-dimensional aquifer in the x - z plane, with dimensional
113 length L_x and uniform dimensional thickness L_z . The aquifer is tilted by
114 an angle θ relative to horizontal. This can be viewed as a cross-section of
115 a sedimentary basin taken perpendicular to a line-drive array of injection
116 wells [28, 4]. We assume that the aquifer is homogeneous and with isotropic
117 permeability.

118 We use the classical model for incompressible fluid flow and advective-
119 dispersive mass transport under the Boussinesq approximation, modeling
120 hydrodynamic dispersion as a Fickian process with a velocity-independent
121 diffusion–dispersion coefficient. The governing equations for this model in
122 dimensionless form are [29]

$$123 \quad \nabla \cdot \mathbf{u} = 0, \tag{1}$$

$$124 \quad \mathbf{u} = -\frac{1}{\mu(c)} (\nabla p - \rho(c)\hat{\mathbf{e}}_g), \tag{2}$$

$$125 \quad \frac{\partial c}{\partial t} = -\mathbf{u} \cdot \nabla c + \frac{1}{\text{Ra}} \nabla^2 c \tag{3}$$

126

127 where p is the scaled pressure deviation from a hydrostatic datum, \mathbf{u} is the
 128 scaled Darcy velocity, and $\hat{\mathbf{e}}_g = (-\sin\theta, -\cos\theta)$ is the unit vector in the
 129 direction of gravity. $\rho(c)$ and $\mu(c)$ are the dimensionless density and viscosity
 130 as functions of the scaled concentration c , as discussed in §2. The Rayleigh
 131 number Ra is given by

$$132 \quad \text{Ra} = \frac{\Delta\rho_m g k L_z}{\phi D_m \mu_m}, \quad (4)$$

133
 134 where g is the body force per unit mass due to gravity, ϕ is porosity, k is the
 135 aquifer permeability, D_m is the diffusion–dispersion coefficient, $\Delta\rho_m$ is the
 136 characteristic density difference driving convective dissolution, and μ_m is the
 137 characteristic viscosity. We write Eqs. (1–3) in dimensional form and give
 138 the complete details of the scaling with which we make them dimensionless
 139 in Appendix A.

140 The behavior of a buoyant gravity current is then completely character-
 141 ized by Eqs. (1–3), the value of Ra , the constitutive laws $\rho(c)$ and $\mu(c)$, and
 142 appropriate initial and boundary conditions.

143 To study convective dissolution from a gravity current, we solve Equa-
 144 tions (1–3) numerically in a rectangular domain of dimensionless height 1
 145 and length $A = L_x/L_z = 20$. We discretize the equations for flow (Eqs. 1–2)
 146 and transport (Eq. 3) in space using 2nd-order finite volumes and 6th-order
 147 compact finite differences (4th order for boundary conditions), respectively,
 148 in a domain of 10000×500 grid blocks (see Appendix B). We evolve this sys-
 149 tem in time using an explicit 3rd-order Runge-Kutta scheme. Perturbations
 150 are triggered by small numerical errors [30].

151 We prescribe the pressure along the right boundary and take the other
 152 boundaries to be impervious. We then write the dimensionless boundary

153 conditions as

$$154 \quad p = 0 \text{ at } x = A \quad (5)$$

$$155 \quad \mathbf{u} \cdot \mathbf{n} = 0 \text{ elsewhere} \quad (6)$$

156
157 for flow, and

$$158 \quad \nabla c \cdot \mathbf{n} = 0 \quad (7)$$

159
160 for transport.

161 Initially, the region $x \leq 4$ is filled with CO_2 . We do not add any per-
162 turbation to trigger the instability. A sequence of snapshots from a typical
163 simulation is shown in Figure 2. These results are qualitatively similar to the
164 fingering patterns observed in experiments using water and propylene glycol,
165 although those fluids have a much higher value of $R \sim 3.7$ [16, 14].

166 4. Effect of dissolution on CO_2 migration

167 We quantify the evolution of the buoyant current with four macroscopic
168 quantities: its mass, its length, the total dissolution rate of CO_2 into the
169 brine, and the average dissolution flux per unit length of the current. These
170 quantities characterize the spreading and migration of the current and the
171 effectiveness of dissolution trapping, which have implications for planning
172 and risk assessment [31, 32].

173 The dissolution flux between two miscible fluids must be defined with
174 care since there is no true interface across which mass is transferred. In-
175 stead, there is an initial concentration distribution that homogenizes as mix-
176 ing progresses. Although the natural characterization for such a system is

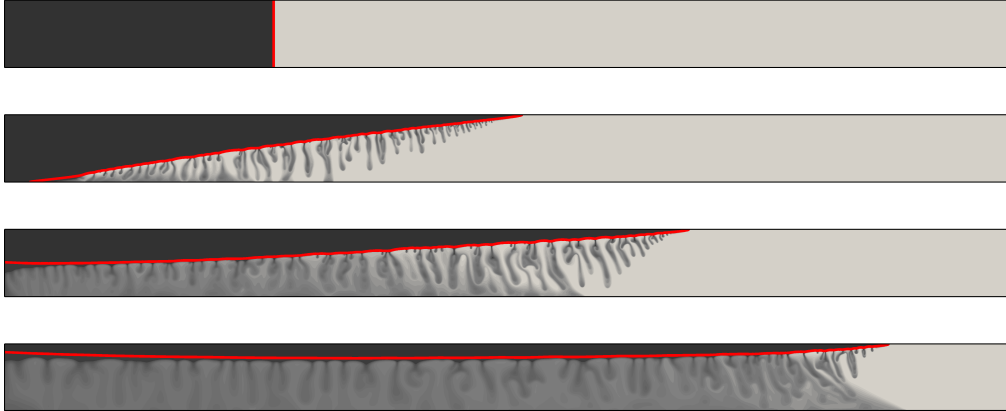


Figure 2: Sequence of snapshots from a high-resolution simulation of convective dissolution from a buoyant current in a sloping aquifer for $Ra = 5000$, $R = 1$, and $\theta = 2.5^\circ$ (not shown) at dimensionless times 0, 3, 9, and 27. The domain extends to $x = 20$, but only $0 \leq x \leq 15$ is shown here. The red line marks the contour of neutrally buoyant concentration $c = c_n$, which separates the buoyant current from the sinking fluid (Fig. 1).

177 through the evolution of the mean scalar dissipation rate [33], it is useful in
 178 practice to define a dissolution flux. Here, we define the dissolution flux via
 179 the non-monotonic behavior of fluid density with concentration. Since mix-
 180 tures with concentration $c = c_n$ are neutrally buoyant relative to the ambient
 181 fluid, this concentration can be used to define a *neutral contour* separating
 182 the buoyant, mobile CO_2 ($c \geq c_n$) from the dense brine with dissolved CO_2
 183 ($c < c_n$; Fig. 1). This is an unstable equilibrium point and any perturbation
 184 of concentration causes significant buoyancy forces that trigger convection.
 185 To define the dissolution flux, we first compute the mass of buoyant fluid as
 186 $M_b(t) = \int_{\Omega_b(t)} c \, d\Omega$, $\Omega_b(t) := \{(x, z) \mid c(x, z, t) > c_n\}$ (Fig. 3a). We then define
 187 the *total dissolution rate* as $-\text{d}M_b/\text{d}t$ (Fig. 3b). By dividing this quantity
 188 by the length of CO_2 -brine interface, which we measure as the length of the

189 neutral contour (Fig. 3c), we obtain the *average dissolution flux* (Fig. 3d).

190 Both the total dissolution rate and the average dissolution flux evolve as
191 the buoyant current migrates (Fig. 3b,d). Much like for a stationary layer
192 of CO₂ dissolving into brine [9, 30, 15, 16, 33, 34], we distinguish three dis-
193 tinct regimes in convective dissolution from the migrating current: a diffusive
194 regime at early times, a constant-flux regime during intermediate times, and
195 a decay at late times. The early-time evolution of the gravity current in this
196 system is a classical lock exchange, where an initially vertical interface be-
197 tween a buoyant fluid and a dense fluid evolves by tilting and stretching (here
198 with the added complication of convective dissolution). The classical sharp-
199 interface model for lock exchange predicts that the length of the interface
200 will grow proportional to $t^{1/2}$ [35]. This regime ceases here when the left-
201 traveling edge of the interface hits the left boundary of the domain, at which
202 point the dynamics of the interface change suddenly as the gravity current
203 detaches from the bottom of the aquifer and enters a migration-dominated
204 regime [36]. Both the dissolution rate and dissolution flux are small at early
205 times as the CO₂-brine interface tilts from its initial, vertical orientation and
206 diffusion–dispersion dominates. After the onset of convection ($t \approx 1$), the
207 dissolution flux becomes roughly constant ($t \approx 1$ –4), as expected for a sta-
208 tionary layer, and the growth of the interface slows down. Before the fingers
209 interact significantly with the bottom boundary, our computed dissolution
210 flux exhibits the same qualitative behavior as has been observed previously
211 for dissolution of a stationary layer [30, 37, 33]. However, our flux differs
212 quantitatively from these previous measurements. This is expected since the
213 value of the flux has been shown to depend strongly on the concentration

214 at which the density maximum occurs [33], and also on the nature of the
215 boundary condition at the boundary where dissolution occurs (here across a
216 moving interface between two miscible fluids *vs.* across a rigid boundary with
217 prescribed concentration) [33, 26]. The total dissolution rate grows strongly
218 during this period since the interface length grows rapidly (Fig. 3c) while
219 the flux remains roughly constant. At later times ($t > 5$), the accumulation
220 of dissolved CO₂ under the leftmost part of the current begins to suppress
221 further convective dissolution there and the average dissolution flux begins to
222 decay (Fig. 3d) [13, 34]. The total dissolution rate also decays (Fig. 3b) even
223 though the length of the interface continues to increase (Fig. 3c), reflecting
224 the fact that the accumulation of dissolved CO₂ is suppressing convective
225 dissolution along a progressively larger fraction of the interface (Fig. 2).

226 As Ra increases, we find that the dynamics of this process converge to a
227 common high-Ra limit, indicating that relevant macroscopic quantities are
228 independent of Ra for Ra \approx 5000 and higher [33]. We therefore fix Ra = 5000
229 in what follows.

230 5. Upscaled model

231 We now consider the extent to which the dynamics of convective dissolu-
232 tion from a migrating gravity current can be captured by a simple upscaled
233 model. Such models have recently been used to develop insight into the
234 physics of CO₂ migration and trapping [38, 39, 36, 18, 40, 19, 12, 41].

235 We have elsewhere presented an upscaled model for the migration and
236 trapping of a buoyant current of CO₂ in a sloping aquifer [12]. The model
237 adopts the sharp-interface approximation, assumes vertical flow equilibrium,

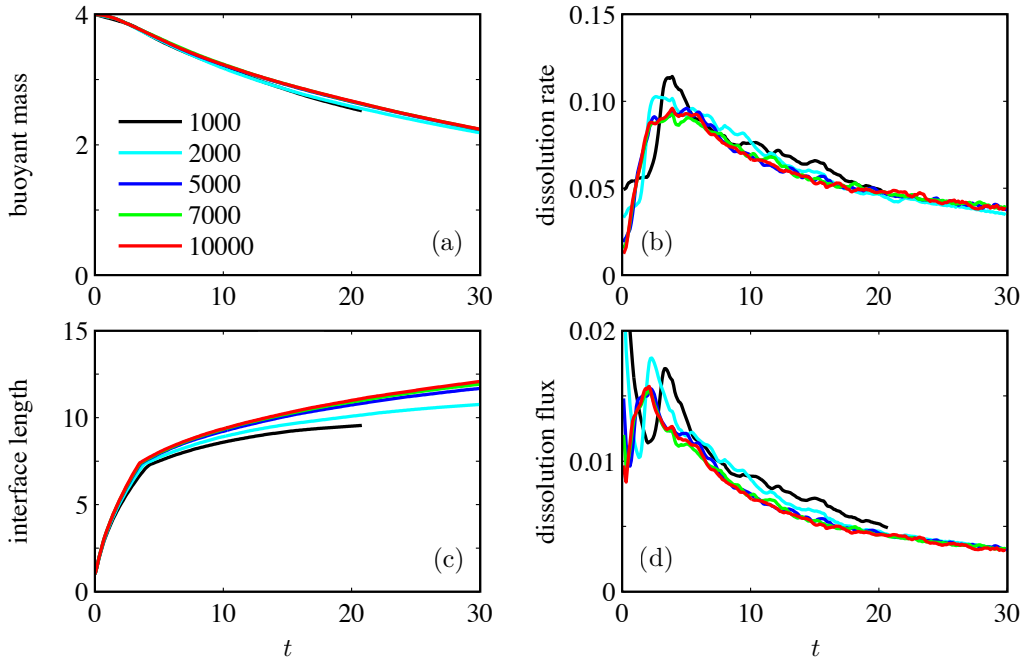


Figure 3: We characterize the dynamics of convective dissolution from a migrating gravity current with the time evolution of four macroscopic quantities: (a) the remaining buoyant mass, $M_b(t)$, (b) the total dissolution rate, $-dM_b/dt$, (c) the length of the CO_2 -brine interface, $L(t)$, measured as the length of the neutral contour, and (d) the average dissolution flux per unit interface length, $-(1/L)dM_b/dt$. Results shown here are for $R = 0$, $\theta = 2.5^\circ$, and several values of Ra , as indicated.

238 and neglects capillarity. The model accounts for residual trapping, but we
 239 ignore this here for simplicity. Here, we extend the model to include the
 240 slumping of the CO₂-rich brine layer against the bottom of the aquifer as in
 241 [13]. We outline the derivation of this model in Appendix C.

242 The model incorporates convective dissolution as a constant flux of CO₂
 243 per unit length of CO₂-brine interface [30, 37, 15, 16, 33]. This rate will decay
 244 as dissolved CO₂ accumulates in the brine beneath the buoyant current, and
 245 we account for this effect by assuming that a dense mound of brine with a
 246 uniform and constant concentration of dissolved CO₂ grows on the bottom of
 247 the aquifer as the buoyant current shrinks. The model is designed to capture:
 248 (1) the decay in dissolution flux by stopping convective dissolution locally
 249 where the dense mound fills the region beneath the buoyant current [12],
 250 and (2) the slumping of the CO₂-rich brine layer against the bottom of the
 251 aquifer [13].

252 The model takes the form of two coupled partial differential equations to
 253 be solved for the local thickness $h(x, t)$ of the buoyant current and the local
 254 thickness $h_d(x, t)$ of the dense mound [12, 13]. We write it in dimensionless
 255 form as

$$256 \quad \frac{\partial h}{\partial t} + \frac{\partial}{\partial x} \left[(1 - f)h \left(N_s - N_g \frac{\partial h}{\partial x} \right) + \delta f h_d \left(N_s + N_g \frac{\partial h_d}{\partial x} \right) \right] = -\tilde{N}_d, \quad (8)$$

$$259 \quad \frac{\partial h_d}{\partial t} + \frac{\partial}{\partial x} \left[-f_d h \left(N_s - N_g \frac{\partial h}{\partial x} \right) - \delta (1 - f_d) h_d \left(N_s + N_g \frac{\partial h_d}{\partial x} \right) \right] = \frac{\tilde{N}_d}{\Gamma_d}, \quad (9)$$

261 where x and t are defined and scaled as in Eqs. (1–3) and h and h_d are
 262 scaled by the aquifer thickness, L_z . The dimensionless parameters N_s , N_g ,
 263 and δ measure the speed of migration due to aquifer slope relative to the

264 speed at which the fingers fall, the speed of buoyant spreading due to gravity
 265 relative to the speed at which the fingers fall, and the migration speed of
 266 the buoyant current relative to that of the dense one, respectively. They are
 267 given by $N_s = (\Delta\rho_{gc}\mu_m \sin \theta)/(\Delta\rho_m\mu_{\text{CO}_2})$, $N_g = (\Delta\rho_{gc}\mu_m \cos \theta)/(\Delta\rho_m\mu_{\text{CO}_2})$,
 268 and $\delta = \Delta\rho_d\mu_{\text{CO}_2}/(\Delta\rho_{gc}\mu_d)$, where $\Delta\rho_{gc}$ is the amount by which the density
 269 of the brine exceeds the density of the buoyant CO_2 , $\Delta\rho_d$ is the amount
 270 by which the density of the mound of brine with dissolved CO_2 exceeds the
 271 density of the ambient brine, μ_{CO_2} is the dynamic viscosity of the CO_2 , μ_d is
 272 the dynamic viscosity of the dense brine with dissolved CO_2 , and q_d is the
 273 volume of CO_2 that dissolves per unit area of CO_2 -brine interface per unit
 274 time. The dissolution flux vanishes locally where the mound of brine with
 275 dissolved CO_2 fills the aquifer beneath the buoyant current:

$$\tilde{N}_d = \begin{cases} N_d & \text{if } h + h_d < 1, \\ 0 & \text{if } h + h_d = 1. \end{cases} \quad (10)$$

276 where $N_d = q_d\mu_m/(\Delta\rho_m g k)$. The volume fraction Γ_d is the equivalent vol-
 277 ume of free-phase CO_2 dissolved in one unit volume of the mound of brine
 278 with dissolved CO_2 . This determines both the rate at which the dense
 279 mound grows and also the density and viscosity of the dense mound via
 280 the constitutive laws for density and viscosity. The fractional-flow func-
 281 tions f and f_d are given by $f(h, h_d) = \mathcal{M}h/[\mathcal{M}h + \mathcal{M}_d h_d + (1 - h - h_d)]$ and
 282 $f_d(h, h_d) = h_d/[\mathcal{M}h + \mathcal{M}_d h_d + (1 - h - h_d)]$, where $\mathcal{M} = \mu_{\text{brine}}/\mu_{\text{CO}_2}$ is the
 283 mobility ratio for the buoyant current (μ_{brine} is the dynamic viscosity of the
 284 brine) and $\mathcal{M}_d = \mu_{\text{brine}}/\mu_d$ is the mobility ratio for the dense mound.

285 All of the parameters in this upscaled model are readily derived from the
 286 parameters and constitutive laws for the full problem with the exception of
 287
 288

289 the upscaled dissolution flux N_d and the volume fraction Γ_d . We measure
 290 the dissolution flux directly from our high-resolution numerical simulations,
 291 taking the dimensionless upscaled flux to be the typical average flux per
 292 unit length before the brine begins to saturate, $N_d \approx 0.015$ (Fig. 3d). We
 293 treat the concentration Γ_d as a fitting parameter, choosing $\Gamma_d \approx 0.18$ as a
 294 value that captures the rate at which the dissolution flux decays as the brine
 295 saturates for $Ra = 5000$ and $R = 0$. Further numerical simulations and
 296 laboratory experiments for a stationary layer and for a migrating current
 297 will be necessary to study the details of this accumulation process to develop
 298 a predictive model for the value of Γ_d . Here, we use these values of N_d and
 299 Γ_d for all comparisons (*i.e.*, $R = 0$ and $R = 1$).

300 We find that this upscaled model captures the evolution of the buoyant
 301 current and also the suppression of convective dissolution under the left
 302 portion of the current as dissolved CO_2 accumulates in the brine (Fig. 4).
 303 Although the dissolution flux in the upscaled model can take only one of
 304 two values locally, $\tilde{N}_d = 0.015$ or 0 (Eq. 10), we find that this is sufficient
 305 to capture the dynamics of the decaying average dissolution flux from the
 306 high-resolution simulations (Fig. 5).

307 6. Conclusions

308 Using high-resolution numerical simulations, we have studied the detailed
 309 dynamics of convective dissolution from a buoyant current of CO_2 in a sloping
 310 aquifer. We have found that, much like for a stationary layer of CO_2 dissolv-
 311 ing into brine, the dissolution flux from a buoyant current is characterized by
 312 three regimes: an early-time diffusive regime before the onset of convection,

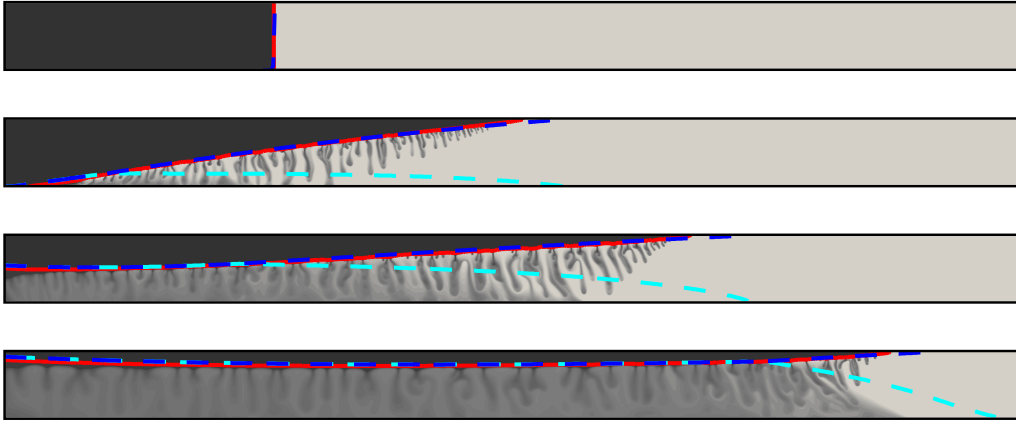


Figure 4: The upscaled model captures the macroscopic shape of the buoyant current. Here, we compare the prediction of the upscaled model (dashed blue line) with the evolution of the neutral contour ($c = c_n = 0.56$, red line) from a high-resolution simulation for $Ra = 5000$, $R = 1$, and $\theta = 2.5^\circ$ at dimensionless times 0, 3, 9, and 27 (same parameters and times as in Fig. 2). Only a portion of the domain is shown ($0 \leq x \leq 15$). The concentration field (black to gray map) show the suppression of the fingering instability by the accumulation of dissolved CO_2 in the brine. We capture this in the upscaled model by disabling convective dissolution locally wherever the dense mound of brine with dissolved CO_2 (dashed cyan line) touches the buoyant current.

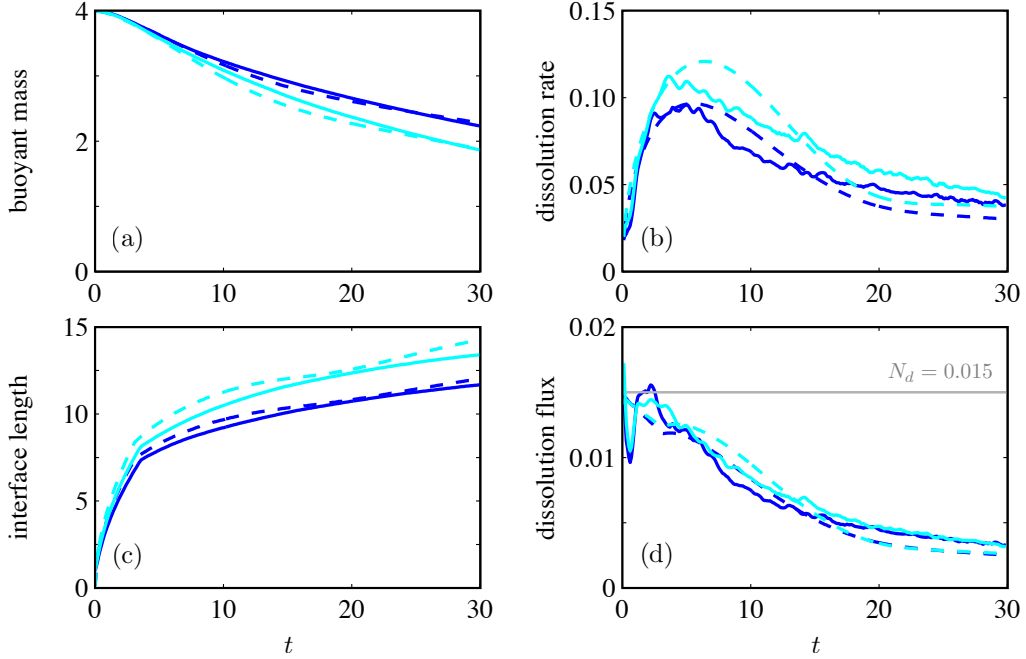


Figure 5: The inclusion of the mound of brine with dissolved CO_2 allows the upscaled model (dashed lines) to capture the decaying average dissolution flux from the high-resolution simulations (solid lines). We again characterize the dynamics of convective dissolution via the time evolution of (a) the remaining buoyant mass, $M_b(t)$, (b) the total dissolution rate, $-\text{d}M_b/\text{d}t$, (c) the length of the CO_2 -brine interface, $L(t)$, and (d) the average dissolution flux, $-(1/L)\text{d}M_b/\text{d}t$. Results shown here are for $\text{Ra} = 5000$, $\theta = 2.5^\circ$, and $R = 0$ (blue) and 1 (cyan).

313 an intermediate constant-flux regime, and a late-time decay as convection
314 is suppressed by the accumulation of dissolved CO₂ in the brine. We have
315 found, further, that these dynamics are independent of Ra for Ra \approx 5000
316 and higher (Fig. 3).

317 We have shown that the macroscopic evolution of the buoyant current
318 can be captured with an upscaled, sharp-interface model that assumes a
319 constant dissolution flux and accounts for the accumulation of dissolved CO₂
320 with a dense mound that grows and slumps on the bottom of the aquifer as
321 the buoyant current shrinks and spreads (Fig. 4). The upscaled dissolution
322 flux q_d is the essential input for upscaled models such as the ones discussed
323 here and elsewhere [12, 11, 13, 14]. Our high-resolution simulations allow
324 us to obtain realistic values for this parameter in the context of a migrating
325 current. The upscaled model also captures the smooth decay in the average
326 dissolution flux even though we use a binary “on-off” model for the flux
327 locally (Fig. 5). These results provide support for insights derived previously
328 from upscaled models based on similar assumptions [12, 11, 13]. In addition,
329 this provides us with a sound base for extending the upscaled model to more
330 complex systems such as heterogeneous aquifers, which will be subject of
331 future work.

332 We have assumed in the upscaled model that dissolved CO₂ accumulates
333 in the brine as a dense mound of constant and uniform CO₂ concentration [12,
334 13]. This concentration determines both the rate at which the dense mound
335 grows and also the rate at which it slumps relative to the ambient brine, and
336 is unknown *a priori*. Here, we have treated this concentration as a fitting
337 parameter. Further high-resolution simulations for a stationary layer and for

338 a migrating current will be necessary to study the details of this accumulation
339 process. At later times, the slumping and down-slope migration of the dense
340 mound will compete with mixing driven by diffusion and dispersion [42].

341 In our high-resolution numerical simulations, we have neglected capillarity
342 and instead assumed that the buoyant fluid and the dense fluid are perfectly
343 miscible, taking advantage of constitutive laws inspired by the analogue fluids
344 that have been used to study convective dissolution in the laboratory [15,
345 16]. This assumption will be reasonable when the capillary pressure is small
346 relative to typical viscous and gravitational pressure changes in the flow. The
347 impact of capillarity on the evolution of gravity currents is increasingly well
348 understood [20, 21, 41, 23, 22]. Recent studies also suggest that capillarity
349 can have a quantitative impact on the dissolution flux [25, 41, 26, 27], but a
350 complete understanding of these effects will require further study including
351 laboratory experiments in addition to mathematical modeling and numerical
352 simulation.

353 Our 2D analogue-fluid model requires a dimensionless density law and
354 three other dimensionless parameters: the Rayleigh number; the log of the
355 mobility ratio; and the aspect ratio of the initial condition. The dimension-
356 less density law can be characterized by two parameters: the concentration
357 at which the density maximum occurs and the ratio of the two density dif-
358 ferences (Fig. 1). The concentration at which the density maximum occurs
359 plays the role of the solubility since convective dissolution will stop as the
360 density of the ambient fluid approaches the maximum attainable density. For
361 the analogue fluids used here, this value is $c_m = 0.26$. Appropriate values
362 for carbon sequestration are 25 to 50 times smaller (~ 0.005 – 0.01 [4]). This

363 means that the brine underlying the CO₂ would saturate with dissolved CO₂
364 much more quickly than in our analogue system. However, the ratio of the
365 density difference that drives the migration of the gravity current to the one
366 that drives convective dissolution is much smaller in the analogue system
367 (~ 3.6) than in the field ($\sim 25\text{--}60$ [4]). This means that a gravity current of
368 supercritical CO₂ in the field would generally migrate faster compared to the
369 rate at which it dissolves than in our analogue-fluid simulations, implying
370 that the saturation of the water beneath the plume will tend to play a lesser
371 role in the field. Similarly, the density-driven migration of the mound of wa-
372 ter with dissolved CO₂ is likely to be much less important in the field since it
373 migrates very slowly compared to the buoyant plume. However, both effects
374 can be extremely important in horizontal or weakly sloping aquifers [12, 13].

375 Reported values of the Rayleigh number in real CO₂ sequestration scenar-
376 ios range over several orders of magnitude, from as low as 100 in thin, low-
377 permeability aquifers to as high as 10^5 in thick, high-permeability aquifers.
378 Our results here target the middle of this range, $Ra \sim 5000$, to explore
379 the limit in which diffusion is still important and to capture the asymptotic
380 behavior for large Ra .

381 The mobility ratio for a real CO₂-brine system is $\mathcal{M} \approx 5\text{--}12$ or $R \approx 1.5\text{--}$
382 2.5 [4], which is somewhat higher than the values used here ($R = 0$ and 1).
383 The mobility ratio has a direct impact on the dynamics of the gravity current,
384 which is longer, thinner, and more strongly tongued for larger R [18, 40]. It
385 also has a weak impact on the magnitude of the dissolution flux, as shown
386 in [33] and in the present work (Fig. 5d).

387 The aspect ratio of the initial condition is the width of the initial rectangle

388 of buoyant fluid relative to the width of the thickness the aquifer, which we
389 take here to be 4. This is a realistic value for carbon sequestration, although
390 field values can range from an order of magnitude smaller (~ 0.4) to an order
391 of magnitude larger (~ 40) depending on the thickness of the aquifer and the
392 volume of CO₂ injected [4].

393 We have confined our modeling and simulations here to two dimensions,
394 but three-dimensional flow effects can be important in scenarios where, for ex-
395 ample, the lateral extent of the plume is not large compared to its length [43].
396 High-resolution simulations combining migration and convective dissolution
397 in 3D, as we have done here in 2D, would be a very interesting follow-up
398 study. Although extension of our modeling to three dimensions is straight-
399 forward, such simulations would be extremely computationally expensive.

400 **7. Acknowledgements**

401 JJH acknowledges the support from the FP7 Marie Curie Actions of
402 the European Commission, via the CO2-MATE project (PIOF-GA-2009-
403 253678). CWM gratefully acknowledges the support of a postdoctoral fel-
404 lowship from the Yale Climate & Energy Institute. RJ acknowledges funding
405 by the US Department of Energy (DE-FE0009738).

406 **Appendix A. Equations in dimensional form**

407 Here we present the 2D mathematical model in dimensional form. We
 408 present the upscaled (1D) mathematical model in dimensional form in Ap-
 409 pendix C.

410 Contrary to the rest of the paper, variables without decoration are di-
 411 mensional and those with tildes are dimensionless. The equations governing
 412 incompressible fluid flow and advective-dispersive mass transport, where we
 413 adopt the Boussinesq approximation and model hydrodynamic dispersion as
 414 a Fickian process, take the form [29]

$$415 \quad \nabla \cdot \mathbf{u} = 0, \quad (\text{A.1})$$

$$416 \quad \mathbf{u} = -\frac{k}{\mu(c)} \left(\nabla p + \rho(c)g \sin \theta \hat{\mathbf{e}}_x + \rho(c)g \cos \theta \hat{\mathbf{e}}_z \right), \quad (\text{A.2})$$

$$417 \quad \phi \frac{\partial c}{\partial t} = -\mathbf{u} \cdot \nabla c + \phi D_m \nabla^2 c, \quad (\text{A.3})$$

418

419 Dimensional Eqs. (A.1–A.3) are related to their dimensionless counterparts
 420 Eqs. (1–3) by the scalings $t = (\phi \mu_m L_z / \Delta \rho_m g k) \tilde{t}$, $\nabla = \tilde{\nabla} / L_z$, $u = (\Delta \rho_m g k / \mu_m) \tilde{u}$,
 421 $p = \Delta \rho_m g L_z \tilde{p} + \rho(c=0)gz + p_0$, $\mu = \mu_m \tilde{\mu}$, and $\rho = \Delta \rho_m \tilde{\rho} + \rho_0$. p_0 and ρ_0 are
 422 a dimensional reference pressure and dimensional brine density, respectively.

423 The density difference $\rho(c = c_m) - \rho(c = 0) = \Delta \rho_m$ drives convective
 424 dissolution, while the density difference $\rho(c = 0) - \rho(c = 1) = \Delta \rho_{gc}$ drives
 425 the migration of the gravity current.

426 **Appendix B. Convergence analysis**

427 Fingering instabilities are very sensitive to numerical discretization [44].
 428 To accurately capture the dynamics of convective dissolution, it is essential

429 for our simulations to resolve the smallest relevant length and time scales.
 430 The smallest such length scale for convective dissolution is believed to be
 431 the critical wavelength for the onset of convection, $\lambda_c \approx 90L_z/\text{Ra}$ [9]. We
 432 present results here for Ra as high as 10000 (Figure 3), for which $\lambda_c/L_z \approx$
 433 0.009. Larger values of Ra require proportionally finer spatial discretizations.
 434 Allocating at least two horizontal grid blocks per wavelength then suggests
 435 a minimum horizontal resolution of ~ 220 grid blocks per unit dimensionless
 436 length for $\text{Ra} = 10000$. We use 500 grid blocks per unit length in both
 437 directions (10000×500 for a domain of 20×1) for all simulations, which we
 438 expect to be sufficient.

439 Regarding the convergence of macroscopic quantities such as the disso-
 440 lution flux, we choose a discretization for which the results vary by a few
 441 percent or less when the grid is refined further. We perform such a conver-
 442 gence analysis by comparing a sequence of simulations performed on meshes
 443 of increasing resolution. We compare resolutions of 200–600 grid blocks per
 444 unit dimensionless length (same in the horizontal and vertical directions).
 445 Since the dimensionless height of the domain is always 1, the resolution is
 446 the same as the number of grid blocks N_z in the vertical direction. We il-
 447 lustrate this convergence quantitatively in Figure B.6 for $\text{Ra} = 5000$, $R = 0$,
 448 and a dimensionless initial width of 1. The domain has aspect ratio $A = 5$,
 449 so the finest mesh has 3000×600 grid blocks ($N_z = 600$). We illustrate this
 450 convergence qualitatively in Figures B.7 and B.8 for $R = 0$ and $R = 1$, re-
 451 spectively. Based on these results, we choose a resolution of 500 grid blocks
 452 per unit length for all simulations presented here as a compromise between
 453 numerical accuracy and computational burden. We expect other parameters,

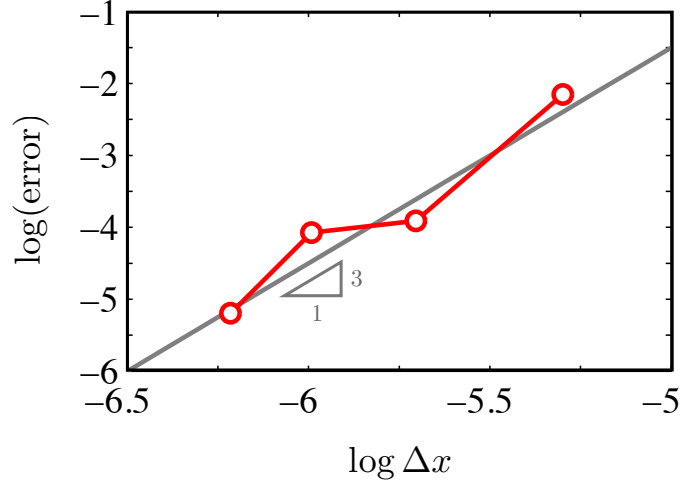


Figure B.6: Numerical convergence of macroscopic quantities with grid size. Here we calculate the error in buoyant mass for grid size Δx as the log of the maximum difference between the value for that grid size and the next coarser one, $\log(\max |M_b^{k+1}(t) - M_b^k(t)|)$. These results are for $R = 0$, $\theta = 0$, and $Ra = 5000$.

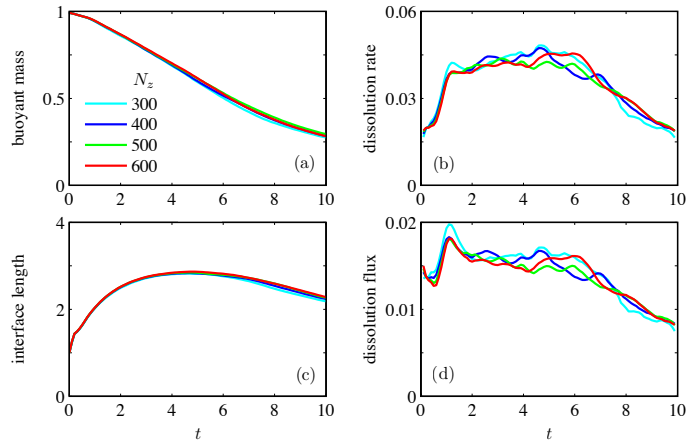


Figure B.7: Convergence with grid size of (a) buoyant mass, (b) total dissolution rate, (c) interface length (length of the neutral contour), and (d) dissolution flux for $Ra = 5000$, $R = 0$, and a dimensionless initial width of 1. These macroscopic quantities converge to within a few percent for $N_z \geq 500$.

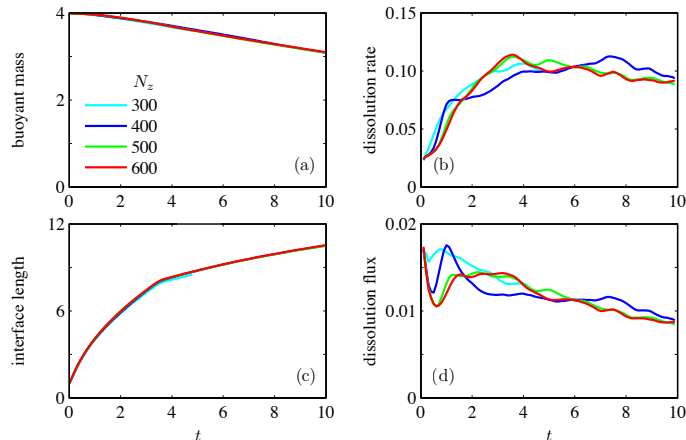


Figure B.8: Convergence with grid size of (a) buoyant mass, (b) total dissolution rate, (c) interface length (length of the neutral contour), and (d) dissolution flux for $Ra = 5000$, $R = 1$, and a dimensionless initial width of 4. As for $R = 0$, these quantities converge to within a few percent for $N_z \geq 500$.

454 such as the slope or the shape of the density curve, to have little impact on
 455 convergence.

456 Appendix C. Derivation of the upscaled model

457 Here we briefly outline the derivation of the upscaled (1D) model in di-
 458 mensional form. This model is an extension of the model of [12] to include
 459 the density-driven slumping of the dense CO_2 -rich brine layer against the
 460 bottom of the aquifer as in [13], but without residual fluids. The model
 461 may also be viewed as an extension of the model of [13] to include slope
 462 and a net background flow. We refer the reader to these previous works for
 463 a detailed discussion and justification of the main assumptions, which in-
 464 clude vertical-flow equilibrium and the sharp-interface approximation. Here,
 465 as in Appendix A and contrary to the rest of the paper, all quantities are

466 *dimensional.*

467 We assume that the fluids are vertically segregated into three regions of
 468 uniform density and viscosity, and that these regions are separated by sharp
 469 interfaces. The three regions contain free-phase CO₂, brine, and brine with a
 470 volume fraction Γ_d of dissolved CO₂. At position x and time t , these regions
 471 have respective thicknesses $h(x, t)$, $h_w(x, t)$, and $h_d(x, t)$, where $h + h_w + h_d =$
 472 L_z . The CO₂ has density ρ_g and viscosity μ_g ; the brine has density ρ_w and
 473 viscosity μ_w ; and the brine with dissolved CO₂ has density ρ_d and viscosity
 474 μ_d .

475 We write the Darcy velocity of the fluid in each region as

$$476 \quad \mathbf{u}_g = -\frac{k}{\mu_g} \left(\nabla p_g + \rho_g g \sin \theta \hat{\mathbf{e}}_x + \rho_g g \cos \theta \hat{\mathbf{e}}_z \right), \quad (\text{C.1})$$

$$477 \quad \mathbf{u}_w = -\frac{k}{\mu_w} \left(\nabla p_w + \rho_w g \sin \theta \hat{\mathbf{e}}_x + \rho_w g \cos \theta \hat{\mathbf{e}}_z \right), \quad (\text{C.2})$$

$$478 \quad \mathbf{u}_d = -\frac{k}{\mu_d} \left(\nabla p_d + \rho_d g \sin \theta \hat{\mathbf{e}}_x + \rho_d g \cos \theta \hat{\mathbf{e}}_z \right), \quad (\text{C.3})$$

479

480 where p_g , p_w , and p_d are the fluid pressures in each region. We next assume
 481 vertical-flow equilibrium, neglecting the vertical component of the fluid ve-
 482 locity relative to the horizontal one because of the characteristic long and
 483 thin nature of the flow. The z -components of Eqs. (C.1–C.3) then imply
 484 that the pressure distribution in each region is hydrostatic and given by

$$485 \quad p_g = p_i(x, t) + \rho_g g \cos \theta (L_z - h - z), \quad (\text{C.4})$$

$$486 \quad p_w = p_i(x, t) + \rho_w g \cos \theta (L_z - h - z), \quad (\text{C.5})$$

$$487 \quad p_d = p_i(x, t) + \rho_w g \cos \theta h_w + \rho_d g \cos \theta (h_d - z), \quad (\text{C.6})$$

488

489 where $p_i(x, t)$ is the unknown pressure along the CO₂ interface ($z = L_z - h$).

490 Substituting Eqs. (C.4–C.6) into the x -components of Eqs. (C.1–C.3) gives
 491 expressions for the horizontal fluid velocity in each region in terms of p_i .

492 Since we have taken the fluids and the rock to be incompressible, the
 493 total volume of fluid flowing through any cross-section of the aquifer must
 494 be conserved. This requirement can be written

$$495 \quad (\mathbf{u}_g \cdot \hat{\mathbf{e}}_x)h + (\mathbf{u}_w \cdot \hat{\mathbf{e}}_x)h_w + (\mathbf{u}_d \cdot \hat{\mathbf{e}}_x)h_d = Q, \quad (\text{C.7})$$

496 where the constant total volume flow rate Q may be nonzero when there
 497 is fluid injection or extraction, leakage, or if there is a natural groundwa-
 498 ter through-flow. Equation (C.7) can be combined with the expressions for
 499 the horizontal fluid velocity obtained from Eqs. (C.1–C.3) and (C.4–C.6) to
 500 eliminate the unknown pressure p_i .

501 Finally, local volume conservation dictates that the change in the thick-
 502 ness of each region must be balanced locally by the divergence of the flux
 503 of fluid through that region and the transfer of volume from one region to
 504 another. This requirement can be written

$$505 \quad \phi \frac{\partial h}{\partial t} + \frac{\partial}{\partial x} [(\mathbf{u}_g \cdot \hat{\mathbf{e}}_x)h] = -\tilde{q}_d, \quad (\text{C.8})$$

$$506 \quad \phi \frac{\partial h_d}{\partial t} + \frac{\partial}{\partial x} [(\mathbf{u}_d \cdot \hat{\mathbf{e}}_x)h_d] = \frac{\tilde{q}_d}{\Gamma_d}, \quad (\text{C.9})$$

507
 508 where \tilde{q}_d is defined by

$$509 \quad \tilde{q}_d = \begin{cases} q_d & \text{if } h + h_d < L_z, \\ 0 & \text{if } h + h_d = L_z. \end{cases} \quad (\text{C.10})$$

510
 511 and q_d is the flux due to convective dissolution, which transfers volume from
 512 the CO_2 -region to the region of brine with dissolved CO_2 . Combining all

513 of the above and eliminating h_w through the requirement that the three
 514 thicknesses sum to the total thickness of the aquifer, the resulting model is
 515 given by

$$\begin{aligned}
 & \frac{\partial h}{\partial t} + \frac{Q}{\phi} \frac{\partial f}{\partial x} + \frac{\Delta\rho_{gc}gk}{\phi\mu_g} \frac{\partial}{\partial x} \left[\sin\theta(1-f)h - \cos\theta(1-f)h \frac{\partial h}{\partial x} \right] \\
 & + \frac{\Delta\rho_dgk}{\phi\mu_d} \frac{\partial}{\partial x} \left[\sin\theta f h_d + \cos\theta f h_d \frac{\partial h_d}{\partial x} \right] = -\tilde{q}_d/\phi,
 \end{aligned} \tag{C.11}$$

$$\begin{aligned}
 & \frac{\partial h_d}{\partial t} + \frac{Q}{\phi} \frac{\partial f_d}{\partial x} + \frac{\Delta\rho_{gc}gk}{\phi\mu_g} \frac{\partial}{\partial x} \left[-\sin\theta f_d h + \cos\theta f_d h \frac{\partial h}{\partial x} \right] \\
 & + \frac{\Delta\rho_dgk}{\phi\mu_d} \frac{\partial}{\partial x} \left[-\sin\theta(1-f_d)h_d - \cos\theta(1-f_d)h_d \frac{\partial h_d}{\partial x} \right] = \frac{\tilde{q}_d}{\phi\Gamma_d},
 \end{aligned} \tag{C.12}$$

521 where $f(h, h_d)$ and $f_d(h, h_d)$ are as defined in §5. Equations (C.11) and (C.12)
 522 are related to their dimensionless counterparts Eqs. (8) and (9) by scaling h
 523 and h_d with characteristic thickness L_z , x with characteristic length L_z , and
 524 t with characteristic time $\phi\mu_m L_z / \Delta\rho_m gk$. Note that we have taken $Q = 0$
 525 in Eqs. (8) and (9) for comparison with our 2D results, in which there is no
 526 net flow.

- 527 [1] S. Bachu, W. D. Gunter, E. H. Perkins, Aquifer disposal of CO₂: Hy-
528 drodynamic and mineral trapping, *Energy Conversion and Management*
529 35 (1994) 269–279.
- 530 [2] K. S. Lackner, Climate change: A guide to CO₂ sequestration, *Science*
531 300 (2003) 1677–1678.
- 532 [3] F. M. Orr Jr., Onshore geologic storage of CO₂, *Science* 325 (2009)
533 1656–1658.
- 534 [4] M. L. Szulczewski, C. W. MacMinn, H. J. Herzog, R. Juanes, Lifetime of
535 carbon capture and storage as a climate-change mitigation technology,
536 *Proceedings of the National Academy of Sciences* 109 (2012) 5185–5189.
- 537 [5] IPCC, Carbon Dioxide Capture and Storage, Special Report prepared by
538 Working Group III of the Intergovernmental Panel on Climate Change,
539 Cambridge, UK (2005).
- 540 [6] G. J. Weir, S. P. White, W. M. Kissling, Reservoir storage and contain-
541 ment of greenhouse gases, *Transport in Porous Media* 23 (1996) 37–60.
- 542 [7] E. Lindeberg, D. Wessel-Berg, Vertical convection in an aquifer column
543 under a gas cap of CO₂, *Energy Conversion and Management* 38 (1997)
544 S229–S234.
- 545 [8] J. Ennis-King, I. Preston, L. Paterson, Onset of convection in anisotropic
546 porous media subject to a rapid change in boundary conditions, *Physics*
547 *of Fluids* 17 (2005) 084107.

- 548 [9] A. Riaz, M. Hesse, H. A. Tchelepi, F. M. Orr Jr., Onset of convection
549 in a gravitationally unstable diffusive boundary layer in porous media,
550 *Journal of Fluid Mechanics* 548 (2006) 87–111.
- 551 [10] K. Pruess, J. Nordbotten, Numerical simulation studies of the long-term
552 evolution of a CO₂ plume in a saline aquifer with a sloping caprock,
553 *Transport in Porous Media* 90 (2011) 135–151.
- 554 [11] S. E. Gasda, J. M. Nordbotten, M. A. Celia, Vertically-averaged ap-
555 proaches for CO₂ migration with solubility trapping, *Water Resources*
556 *Research* 47 (2011) W05528.
- 557 [12] C. W. MacMinn, M. L. Szulczewski, R. Juanes, CO₂ migration in saline
558 aquifers. Part 2. Capillary and solubility trapping, *Journal of Fluid Me-*
559 *chanics* 688 (2011) 321–351.
- 560 [13] C. W. MacMinn, J. A. Neufeld, M. A. Hesse, H. E. Huppert, Spread-
561 ing and convective dissolution of carbon dioxide in vertically confined,
562 horizontal aquifers, *Water Resources Research* 48 (2012) W11516.
- 563 [14] C. W. MacMinn, R. Juanes, Buoyant currents arrested by convective dis-
564 solution, *Geophysical Research Letters* Doi:10.1002/grl.50473. *In press.*
- 565 [15] J. A. Neufeld, M. A. Hesse, A. Riaz, M. A. Hallworth, H. A. Tchelepi,
566 H. E. Huppert, Convective dissolution of carbon dioxide in saline
567 aquifers, *Geophysical Research Letters* 37 (2010) L22404.
- 568 [16] S. Backhaus, K. Turitsyn, R. E. Ecke, Convective instability and mass
569 transport of diffusion layers in a Hele-Shaw geometry, *Physical Review*
570 *Letters* 106 (2011) 104501.

- 571 [17] R. Juanes, E. J. Spiteri, F. M. Orr, M. J. Blunt, Impact of relative
572 permeability hysteresis on geological CO₂ storage, *Water Resources Re-*
573 *search* 42 (12) (2006) W12418.
- 574 [18] M. A. Hesse, F. M. Orr Jr., H. A. Tchelepi, Gravity currents with resid-
575 ual trapping, *Journal of Fluid Mechanics* 611 (2008) 35–60.
- 576 [19] C. W. MacMinn, M. L. Szulczewski, R. Juanes, CO₂ migration in saline
577 aquifers. Part 1. Capillary trapping under slope and groundwater flow,
578 *Journal of Fluid Mechanics* 662 (2010) 329–351.
- 579 [20] J. M. Nordbotten, H. K. Dahle, Impact of the capillary fringe in verti-
580 cally integrated models for CO₂ storage, *Water Resources Research* 47
581 (2011) W02537.
- 582 [21] M. J. Golding, J. A. Neufeld, M. A. Hesse, H. E. Huppert, Two-phase
583 gravity currents in porous media, *Journal of Fluid Mechanics* 678 (2011)
584 248–270.
- 585 [22] M. J. Golding, H. E. Huppert, J. A. Neufeld, The effects of capillary
586 forces on the axisymmetric propagation of two-phase, constant-flux grav-
587 ity currents in porous media, *Physics of Fluids* 25 (2013) 036602.
- 588 [23] B. Zhao, C. W. MacMinn, M. L. Szulczewski, J. A. Neufeld, H. E.
589 Huppert, R. Juanes, Interface pinning of immiscible exchange flows in
590 porous media, *Physical Review E* 87 (2013) 023015.
- 591 [24] F. Doster, J. M. Nordbotten, M. A. Celia, Impact of capillary hysteresis
592 and trapping on vertically integrated models for CO₂ storage, *Advances*
593 *in Water Resources* *Submitted for publication in this issue.*

- 594 [25] M. T. Elenius, J. M. Nordbotten, H. Kalisch, Effects of a capillary tran-
595 sition zone on the stability of a diffusive boundary layer, *IMA Journal*
596 *of Applied Mathematics* 77 (6) (2012) 771–787.
- 597 [26] D. R. Hewitt, J. A. Neufeld, J. R. Lister, Convective shutdown in a
598 porous medium at high Rayleigh number, *Journal of Fluid Mechanics*
599 719 (2013) 551–586.
- 600 [27] B. Li, H. A. Tchelepi, S. M. Benson, Influence of capillary entry pressure
601 on CO₂ solubility trapping, *Advances in Water Resources* *Submitted for*
602 *publication in this issue.*
- 603 [28] J.-P. Nicot, Evaluation of large-scale CO₂ storage on fresh-water sections
604 of aquifers: An example from the Texas Gulf Coast Basin, *International*
605 *Journal of Greenhouse Gas Control* 2 (2008) 582–593.
- 606 [29] M. Ruith, E. Meiburg, Miscible rectilinear displacements with gravity
607 override. Part 1. Homogeneous porous medium, *Journal of Fluid Me-*
608 *chanics* 420 (2000) 225–257.
- 609 [30] J. J. Hidalgo, J. Carrera, Effect of dispersion on the onset of convection
610 during CO₂ sequestration, *Journal of Fluid Mechanics* 640 (2009) 441–
611 452.
- 612 [31] E. J. Wilson, S. J. Friedmann, M. F. Pollak, Research for deployment:
613 Incorporating risk, regulation, and liability for carbon capture and se-
614 questration, *Environmental Science & Technology* 41 (2007) 5945–5952.
- 615 [32] C. J. Seto, G. J. McRae, Reducing risk in basin scale CO₂ sequestration:

- 616 A framework for integrated monitoring design, *Environmental Science*
617 & *Technology* 45 (2011) 845–859.
- 618 [33] J. J. Hidalgo, J. Fe, L. Cueto-Felgueroso, R. Juanes, Scaling of convec-
619 tive mixing in porous media, *Physical Review Letters* 109 (2012) 264503.
- 620 [34] A. C. Slim, M. M. Bandi, J. C. Miller, L. Mahadevan, Dissolution-driven
621 convection in a Hele-Shaw cell, *Physics of Fluids* *To appear*.
- 622 [35] H. E. Huppert, A. W. Woods, Gravity-driven flows in porous layers,
623 *Journal Of Fluid Mechanics* 292 (1995) 55–69.
- 624 [36] M. A. Hesse, H. A. Tchelepi, B. J. Cantwell, F. M. Orr Jr., Gravity
625 currents in horizontal porous layers: Transition from early to late self-
626 similarity, *Journal of Fluid Mechanics* 577 (2007) 363–383.
- 627 [37] G. S. H. Pau, J. B. Bell, K. Pruess, A. S. Almgren, M. J. Lijewski,
628 K. Zhang, High-resolution simulation and characterization of density-
629 driven flow in CO₂ storage in saline aquifers, *Advances in Water Re-*
630 *sources* 33 (2010) 443–455.
- 631 [38] S. Lyle, H. E. Huppert, M. Hallworth, M. Bickle, A. Chadwick, Axisym-
632 metric gravity currents in a porous medium, *Journal of Fluid Mechanics*
633 543 (2005) 293–302.
- 634 [39] J. M. Nordbotten, M. A. Celia, Similarity solutions for fluid injection
635 into confined aquifers, *Journal of Fluid Mechanics* 561 (2006) 307–327.
- 636 [40] R. Juanes, C. W. MacMinn, M. L. Szulczewski, The footprint of the
637 CO₂ plume during carbon dioxide storage in saline aquifers: Storage

- 638 efficiency for capillary trapping at the basin scale, *Transport in Porous*
639 *Media* 82 (2010) 19–30.
- 640 [41] S. E. Gasda, J. M. Nordbotten, M. A. Celia, Application of simplified
641 models to CO₂ migration and immobilization in large-scale geological
642 systems, *International Journal of Greenhouse Gas Control* 9 (2012) 72–
643 84.
- 644 [42] M. L. Szulczewski, R. Juanes, The evolution of miscible gravity currents
645 in horizontal porous layers, *Journal of Fluid Mechanics* *doi:?*
- 646 [43] J. M. Nordbotten, B. Flemisch, S. E. Gasda, H. M. Nilsen, Y. Fan, G. E.
647 Pickup, B. Wiese, M. A. Celia, H. K. Dahle, G. T. Eigestad, K. Pruess,
648 Uncertainties in practical simulation of CO₂ storage, *International Jour-*
649 *nal of Greenhouse Gas Control* 9 (2012) 234–242.
- 650 [44] R. A. Schincariol, F. W. Schwartz, C. A. Mendoza, On the generation
651 of instabilities in variable density flow, *Water Resources Research* 30
652 (1994) 913–927.